Eur. Phys. J. B **11**, 243–254 (1999)

THE EUROPEAN PHYSICAL JOURNAL B

EDP Sciences
© Società Italiana di Fisica
Springer-Verlag 1999

Canted antiferromagnetism and magnetoelastic coupling in metallic $Ho_{0.1}Ca_{0.9}MnO_3$

K. Hagdorn[1], D. Hohlwein[1,2], J. Ihringer[1], K. Knorr[1], W. Prandl[1,a], H. Ritter[1], H. Schmid[1], and Th. Zeiske[1,2]

[1] Institut für Kristallographie, Universität Tübingen, Charlottenstrasse 33, 72070 Tübingen, Germany
[2] Hahn-Meitner-Institut, Glienicker Strasse 100, 14109 Berlin, Germany

Received 21 January 1999

Abstract. $Ho_{0.1}Ca_{0.9}MnO_3$ is a canted antiferromagnet with the magnetic space group Pn′ma′. The magnetic structure is a superposition $C_xF_yA_z$ of the three types of order allowed in Pn′ma′. In the Ca-rich corner of the system $Ho_{1-x}Ca_xMnO_3$ the title compound has a strong magnetoelastic distortion $\Delta V_{MAG}/V = 1.2 \times 10^{-3}$, the highest metallic conductivity and a ferromagnetic component F_y close to the maximum in the series. Among the areas *ab*, *bc*, *ca* calculated from the lattice constants only *ca* shows a strong magnetoelastic effect below $T_N = 106$ K. The *x*-, *y*-, *z*-spin components depend differently on the temperature. This gives rise to spin rotation which is particularly strong close to T_N. MnO_6 octahedra have short bond lengths with a temperature independent average $\langle MnO \rangle = 1.91$ Å. They are practically regular at room temperature and show a Jahn-Teller distortion of 3.5% in the magnetically ordered state. Above T_N we find small polaron conductivity. The presence of the Jahn-Teller distortion due to the only small abundance (10%) of Mn^{3+} in the $t_{2g}^3e_g$ configuration is attributed to delocalised e_g electrons. In the magnetically ordered state the averaged magnetic moment of Mn is reduced appreciably from the paramagnetic value due to spin disorder.

PACS. 75.25.+z Spin arrangements in magnetically ordered materials (including neutron and spin-polarized electron studies, synchrotron-source x-ray scattering, etc.) – 71.38.+i Polarons and electron-phonon interactions – 71.30.+h Metal-insulator transitions and other electronic transitions

1 Introduction

Jonker and van Santen reported 1950 in two seminal papers [1,2] about ferromagnetism and metallic conductivity in the perovskitic oxides $(La, Me)MnO_3$ with Me = Ca, Sr and Ba. These phenomena where then attributed to double exchange and electron hopping [3–5]. Wollan and Koehler [6] investigated the microscopic magnetism of $(La, Ca)MnO_3$ mixed crystals and found a wealth of magnetic structures. The discovery of magnetoresistance [7] in $(La, Ca)MnO_3$ triggered much renewed interest in the magnetic and transport phenomena of this class of metallic or semiconducting ferromagnets with orthorhombically distorted perovskite structure.

Recently compositions with giant magnetoresistance [8–12] have been found in this family of compounds and the question about the origin of this effect as well as possible technical applications of these materials for magnetic sensors have greatly encouraged the efforts to increase the magnitude of the effect. In all these attempts chemical engineering was the basic working principle: La is replaced partly or completely by one or more of the light rare earth elements [10–12]. The crystal chemical reason is that $LaMnO_3$, $REMnO_3$ (for the light rare earth ions from Ce to Dy) and $CaMnO_3$ all have the distorted perovskite structure with the space group Pnma and form continuous series of isomorphous mixed crystals [13–15]. Crystals of $REMnO_3$ with heavy RE ions from Ho to Lu on the other hand crystallize hexagonally [16] with the space group $P6_3cm$ at atmospheric pressure, but can be transformed at $T \approx 900\,℃$ and high pressure into the orthorhombic form [17]. In the case of $HoMnO_3$ the volume shrinks in the transition from the hexagonal to the orthorhombic phase by $\Delta V/V = 9.4\%$.

Since the ionic radii of Ca^{++} (0.99 Å) and Ho^{3+} (0.894 Å) differ by barely more than the empirical compatibility ratio $\Delta r/r \leq 10\%$ for isomorphous structures, mixed crystals $Ho_{1-x}Ca_xMnO_3$ should have the Pnma structure at least for x not too close to zero, and this is indeed what we find: single orthorhombic phases at least up to $x = 0.5$, and a mixture of orthorhombic as well as hexagonal crystals at $x = 0.9$ (300 K). Since the Ho^{3+} ion is smaller than Ca^{++}, whereas $r_{La^{3+}} = 1.016$ Å comes close to $r_{Ca^{2+}}$, one would expect differences in the magnetic phase diagram if the ionic radii were the driving force, but none if stoichiometry is the governing factor. Indeed for any ion, La^{3+} or RE^{3+}, in a compound $(A_{1-x}^{3+}Ca_x^{2+})MnO_3 = (A_{1-x}^{3+}Ca_x^{2+})(Mn_{1-x}^{3+}Mn_x^{4+})O_3$ the homogeneous population of Mn^{4+} with the electron

[a] e-mail: wolfram.prandl@uni-tuebingen.de

configuration t_{2g}^3 for $x = 1$ is changed into a mixed valence state $(t_{2g}^3 e_g)_{1-x}(t_{2g}^3)_x$ for $x < 1$. The present paper provides evidence for the influence of the ionic radii on the magnetic behaviour.

The paper is organised in the following way: in Section 2 we present the experimental details, in Section 3.1 basic information on the structure, and in 3.2 and 3.3 the results of neutron and high resolution X-ray powder diffraction, respectively. Section 3.4 covers the temperature dependent atomic shifts, and 4 gives a summary. We refer to our magnetisation and resistivity measurements in Section 3.2.

2 Experimental details

Samples of $Ho_{0.1}Ca_{0.9}MnO_3$ were obtained by standard ceramic techniques. Calcium carbonate and metal oxides of Ho and Mn were ground, pressed into pellets and calcined at 1 000 ℃ in air. This procedure was repeated once, and in the final step the samples were annealed in pure oxygen at 1 400 ℃ (24 h) and at 700 ℃ (15 h).

X-ray powder diagrams were taken with a focusing low temperature Guinier-diffractometer and camera [18] using CuKα_1 radiation. Most of the data were recorded on X-ray films, but a few diagrams were measured with a twin counter. All samples contained ≈ 5 weight % of Si (NBS 640 B; average particle size 5 μm) as a calibration standard.

Measurements were made in the temperature interval 10 K $\leq T \leq$ 290 K with linear heating/cooling slopes of 10 K/h. The powder samples were prepared on circular mylar sheets which were rotated with 6 revolutions/min in the X-ray beam in order to guarantee good grain statistics of the powder.

We used a film lift device for the temperature dependent measurements: the film is moved with constant speed behind a cylindrical aperture of 2 mm height. The magnitude of the aperture, the speed of the film motion and the slope for changing the temperature imply an uncertainty $\Delta T \approx 1$ K for a specific position of the film.

Intensities on the films were digitised with a JOECE-LOEBL densitometer (series 1471; resolution of the optical density: 10 bits) in tracks separated by 5 K each. Lattice constants scaled with the lattice constant $a_{Si}(T)$ [19] were extracted with the local profile refinement procedure SIMREF 2.4 [20].

Neutron powder diffraction data were recorded at the E2/1 Flat-Cone and powder diffractometer [21] of the Berlin Neutron Scattering Center/HMI/Berlin. We used neutrons with a wavelength of 2.41 Å from the (002) planes of a pyrolytic graphite monochromator. Higher harmonics were suppressed by a graphite filter in the primary beam. The diffractometer is equipped with a linear position sensitive detector (400 channels) covering 80° in 2Θ. The pixel resolution of 0.2° in 2Θ is improved by an automatic angular shift of the detector by 0.1° in 2Θ. In this way the density of data points is doubled: this is important for the Rietveld refinements. The angular range covered was $15° < 2\Theta < 95°$. To reduce the angular width of the Bragg reflections the horizontal divergence of the incoming neutron beam is limited by a 30′ Soller collimator mounted in front of the monochromator. An oscillating radial collimator installed between the sample and the multidetector is used to improve the signal to background ratio and to eliminate scattering due to the cryostat. The powdered samples are contained in a cylindrical vanadium can (diameter: 8 mm) mounted in an ILL orange cryostat. Measurements were made in the temperature interval between 10 K and 150 K. The data collection at each temperature required about 3 hours.

3 Results

3.1 Basic structural data

The crystal structure of $Ho_{0.1}Ca_{0.9}MnO_3$ is related to the ideal cubic perovskite structure by tilting the MnO_6 octahedra. The specific tilt system active in the present case is $a-b+a-$ in Glazer's notation [22] for our choice of axes. The resulting orthorhombic O-type structure with space group Pnma has lattice constants $a \approx \sqrt{2}a_P$, $b \approx 2a_P$, $c \approx \sqrt{2}a_P$ with $a > c$ and $b > c\sqrt{2}$. Orthorhombically distorted perovskites obeying $b > c\sqrt{2}$ are described as the O type, and as O′ type for $b < c\sqrt{2}$ in the literature [15].

The manganese ions occupy the 4a Wyckoff positions (0, 0, 0; 1/2, 0, 1/2; 0, 1/2, 0;1/2, 1/2, 1/2) [23]. Ho/Ca and O_1 are in 4c positions $(x, 1/4, z)$ and O_2 in the general 8d position (x, y, z). For the description of the magnetic structure we use the standard labels [24] $A_\alpha(+--+)$, $C_\alpha(++--)$ and $F_\alpha(++++)$, where the signs refer to the α $(= x, y, z)$-component of the magnetic moments of the Mn ions in 4a in the order given.

3.2 Neutron diffraction: magnetism

Below ≈ 100 K the neutron diagrams show, beyond the allowed nuclear reflections, two features: purely magnetic reflections and additional intensity on top of nuclear peaks (Figs. 1a and 1b). All magnetic contributions can be indexed in the chemical cell, *i.e.* with the wave vector $\mathbf{q} = (0, 0, 0)$. The two observations mentioned point out a superposition of ferro- and antiferromagnetic components, *i.e.* due to a canted antiferromagnet. All data can indeed be interpreted with the magnetic space group Pn′ma′ [25] which supports a magnetic structure of the type $(C_xF_yA_z)$. A refinement based on Pn′ma′ is shown in Figure 1b. Magnetic and structural data calculated with the profile refinement program FULLPROF 2.2 [26] are given in Table 1.

The superimposed (110)/(011) reflections are predominantly of antiferromagnetic origin due to the A_z component: (110) is purely magnetic, whereas (011) has a very small calculated nuclear contribution, which amounts to $I(011)_{\text{nuclear}}/[I(110) + I(011)]_{\text{total}} = 2.5 \times 10^{-3}$ at 10 K. The two reflections occur at $2\Theta_{(110)} = 32.131°$

Table 1. Structural and magnetic parameters at 10 K.

space group:	Pnma			
magnetic space group:	Pn′ma′			
magnetic structure:	$C_xF_yA_z$			
lattice constants:	$a = 5.301\,9(1)$ Å			
	$b = 7.451\,5(2)$ Å			
	$c = 5.260\,5(1)$ Å			
	Wyckoff position	x	y	z
Ho/Ca	4*b*	0.042(2)	0.25	0.488(3)
O_1	4*c*	−0.005(2)	0.25	0.075(2)
O_2	8*d*	0.282(2)	0.035(1)	−0.207(2)
Mn	4*a*	0.0	0.0	0.0
magnetic moment[(1)] [μ_B]		0.375(30)	0.895(80)	2.064 (20)

[(1)] the absolute values $|m_x|$, $|m_y|$, $|m_z|$ at Mn(0, 0, 0) are given. The four different orientations of the magnetic moment compatible with the data are discussed in Section 4 (see also Fig. 15).

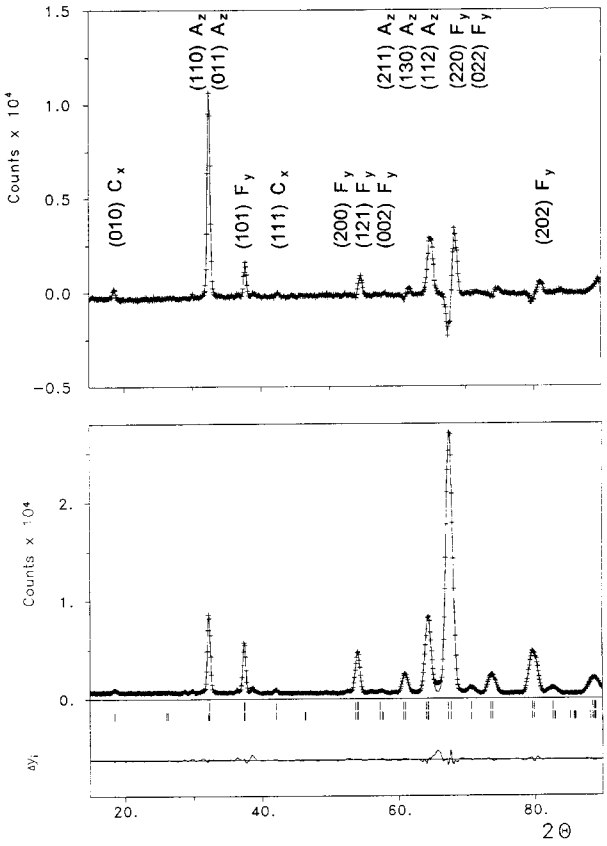

Fig. 1. (a) Difference diagram $I_{10\ K} - I_{150\ K}$: the ferromagnetic intensities sitting on top of allowed nuclear reflections of Figure 1a are clearly visible. Additional magnetic reflections are due to the canted AF components in the ordered phase. (b) A fit of the 10 K data by the model of the canted antiferromagnet.

and $2\Theta_{(011)} = 32.305°$, respectively: they can not be separated with the resolution at hand. Indeed at $T > T_N$ no nuclear intensity can be found at the position given, and so the total intensity may safely be taken as purely antiferromagnetic due to the A_z component.

Since the (110)/(011) peaks are well separated from other reflections their intensity can be extracted with good accuracy: we find $(\sigma_I/I) = 8\times10^{-3}$ and 1.3×10^{-2} at 10 K and 90 K, respectively: Figure 2 (bottom). For fitting the (110)/(011) integrated intensity we use a phenomenological formula

$$I(T) = C(1-\tau^d)^e \tag{1}$$

with $\tau = T/T_N$ which describes the observed M^2 (A_z) quite reasonably: Figure 2.

In the limit $T \Longrightarrow T_N$ equation (1) becomes

$$I(T) \sim M^2 \sim d^e(1-\tau)^e, \tag{2}$$

and for low temperatures $T \Longrightarrow 0$

$$I(T) = C(1-de\tau^d). \tag{3}$$

So we obtain for the sublattice magnetisation $M \sim I^{1/2}$

$$\Delta M = M(0) - M(T) \sim T^d$$

in the latter case.

Fitting the data with this model we find $T_N = 106.0(0.14)$ K, $e = 0.736(0.020)$ and $d = 2.53(0.09)$.

Close to T_N this results in $M \sim (1-\tau)^{e/2}$ with $e/2 = 0.368(.010)$ which is very close to the critical exponent $\beta = 0.364\,6$ of the 3-d Heisenberg ferromagnet [27]. On the other hand we obtain for low temperatures $\Delta M \sim T^{2.53(9)}$, while from spin wave theory one would expect $\Delta M \sim T^2$ for an isotropic Heisenberg antiferromagnet [28]. The larger exponent of the power law found experimentally may be a hint for the contribution of the local anisotropy to the spin wave dispersion or be due to magnetoelastic interaction. The magnetic structure found is given in Figure 3.

We derive the temperature dependence of the spin components (Fig. 4) from a combination of profile

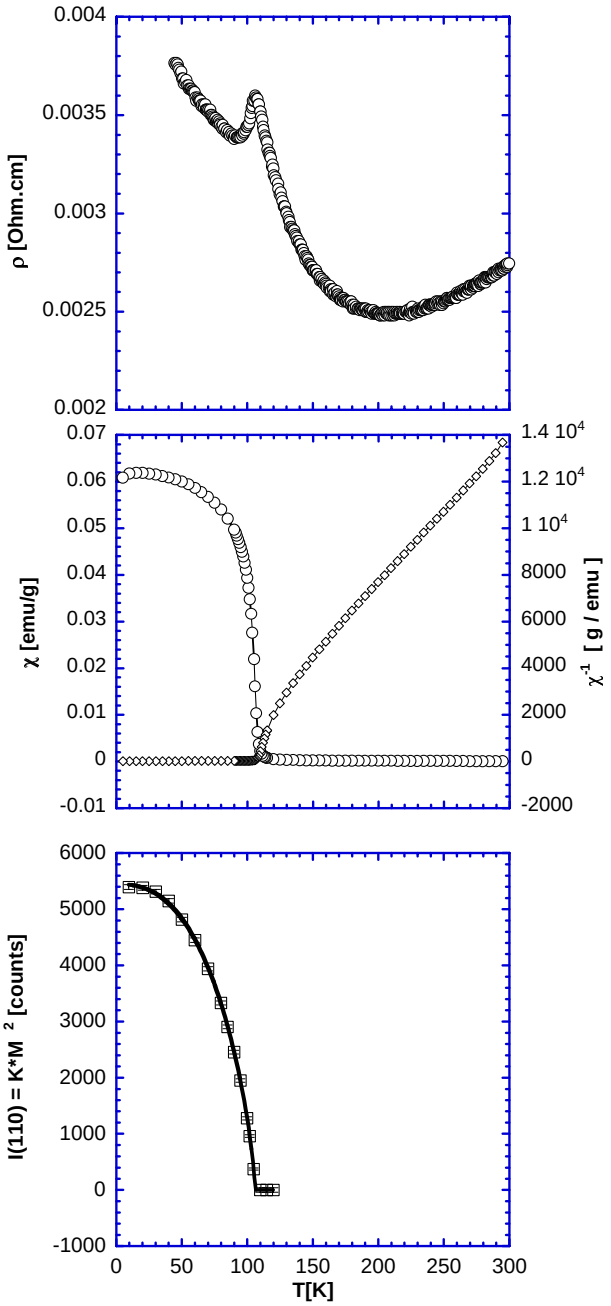

Fig. 2. The temperature dependence of the susceptibility χ and its inverse, of the resistivity ρ and of the magnetic intensity $I(110/011)$.

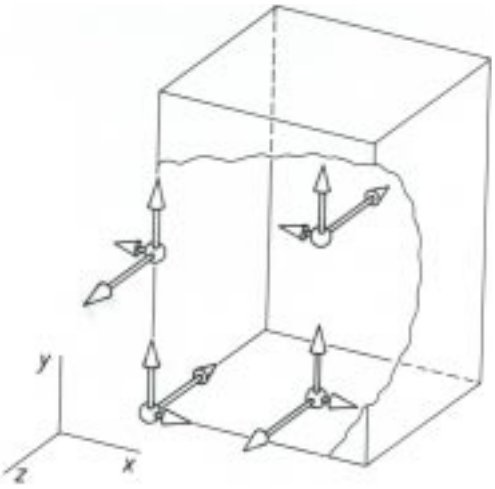

Fig. 3. The magnetic structure at 10 K. In the structure shown the magnetic moment at $\mathrm{Mn}(0,0,0)$ is $(|m_x|, |m_y|, -|m_z|)$. For variants compatible with the data see Figure 15 and the discussion in Section 4.

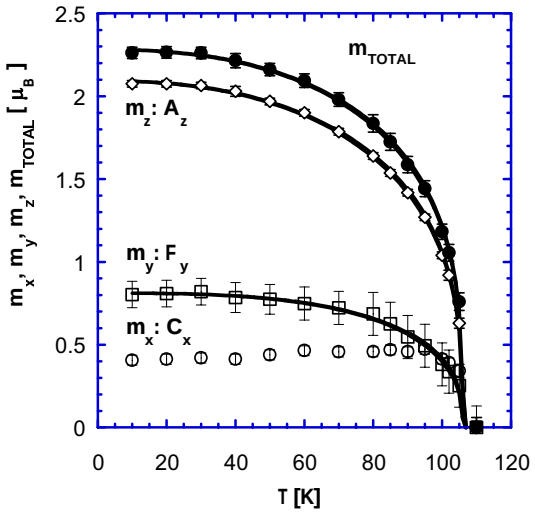

Fig. 4. The temperature dependence of m_x, m_y, m_z, and m_{total}. The three components clearly behave differently. Fit parameters: Table 1.

refinements of the neutron data and a direct analysis of the mixed ferromagnetic and nuclear reflections (020) and (121). It may be worth while to point out here that a straightforward application of only the profile refinement method at all temperatures would result in an erroneous temperature dependence of the ferromagnetic component m_y for values of m_y close to zero: m_y would vanish smoothly close to 95 K, well below T_{N}. This is due to the fact that in the diffraction of unpolarized neutrons magnetic and nuclear *intensities* are superimposed. If the ferromagnetic contribution to the complete data set is very small or zero, then it will have negligible influence on the residual of the whole powder pattern which is minimised during the refinement. The antiferromagnetic sublattice magnetisations m_x and m_z, on the other hand, give rise to some pure magnetic reflections, and so are not touched by this difficulty. We underline this argument by Figure 2 which shows the magnetisation (properly speaking $\chi = M/H$ for a powder sample in a field of 100 Oe; [29]) and the resistivity $\rho(T)$ [30]. For $\rho(T)$ we find the anomaly typical for the giant magnetoresistant compounds: a maximum at $T_{\mathrm{N}} = 106$ K. The magnetisation vanishes, again at the same temperature. These independent observations support the method used for the determination of the ferromagnetic component from neutron data. The observed susceptibility contains two contributions: a holmium and a manganese part. Neutron measurements down to 50 mK do not give any evidence for Ho spin order. We have

Table 2. Fit of magnetic and lattice data with equation (1): $A\left[1-(T/T_0)^d\right]^e$. Parameters given without errors were kept constant.

	A	T_0 [K]	d	e
$I_{(110)+(011)}$		106.0 (0.14)	2.53 (0.09)	0.736 (0.02)
m_x [μ_B]	0.375 (0.024)$^{(1)}$	-	-	-
	-	-	-	-
m_y [μ_B]	0.895 (0.074)$^{(1)}$	106.0	-	-
	0.81 (0.05)$^{(2)}$	-	3.0 (2.2)$^{(2)}$	0.37 (0.16)$^{(2)}$
m_z [μ_B]	2.064 (0.024)$^{(1)}$	106.0	-	-
	2.09 (0.01)$^{(2)}$	-	2.32 (0.16)$^{(2)}$	0.33 (0.01)$^{(2)}$
m_{total} [μ_B]	2.28 (0.04)$^{(1)}$	106.0	-	-
	2.28 (0.02)$^{(2)}$	-	2.38 (0.30)$^{(2)}$	0.31 (0.02)$^{(2)}$
ΔV_m [Å^3]	−0.276 (0.036)	106.1 (1.6)	1.10 (0.54)	0.66 (0.14)
Δa [Å]	−0.0043 (0.0001)	101.4 (2.2)	2.48 (0.43)	0.95 (0.21)
Δb [Å]	0.0074 (0.0002)	100.6 (1.4)	2.29 (0.36)	0.99 (0.15)
Δc [Å]	−0.0042 (0.0001)	106.0	2.51 (0.42)	0.84 (0.10)

(1) from FULLPROF [23].

(2) from equation (1) applied to the temperature dependent FULLPROF results.

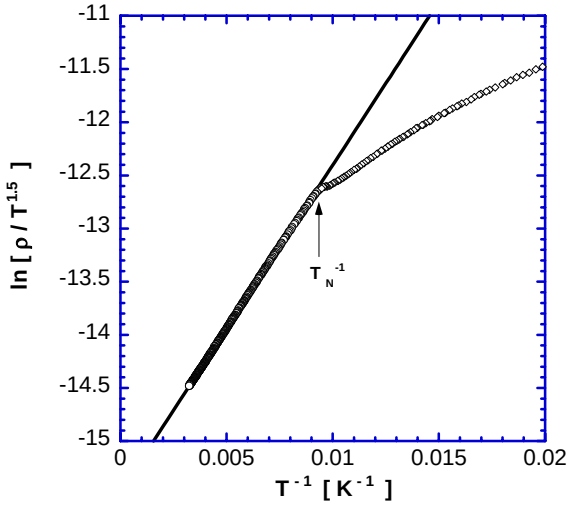

Fig. 5. The fit of the high temperature resistivity with the small polaron law, equation (4).

modelled the paramagnetic Ho contribution $\chi_{Ho}(T)$ with an approximate cubic crystal field which turned out to be necessary in order to make the manganese susceptibility positive at all temperatures [29]. From the corrected $\chi_{Mn}(T) = \chi_{exp}(T) - \chi_{Ho}(T)$ we obtain a paramagnetic Curie temperature $\Theta_C \approx 99$ K and a Mn mean square magnetic moment $\langle\mu^2_{Mn}\rangle^{1/2} \approx 3.3\ \mu_B$.

The resistivity due to small polarons is [31]

$$\rho(T) = AT^{3/2}\exp(T_{SP}/T). \quad (4)$$

In Figure 5 we have plotted $\ln[\rho(T)/T^{3/2}]$ *vs.* $1/T$. As shown the high temperature small polaron part above T_N can be fitted fairly well with a straight line: from this we obtain a small polaron activation energy $T_{SP} = 307.4(0.2)$ K. We may point out that the minimum of $\rho(T)$ in Figure 2 does apparently not have any physical significance, since it is completely absorbed in the straight line section of Figure 5.

Since the ferromagnetic intensity is always on top of nuclear reflections the component $m_y(F_y)$ have larger error bars. The total local magnetisation is dominated by the antiferromagnetic component $m_z(A_z)$, and so it is not surprising that m_{total} can be fitted with equation (1) also. The resulting exponents d and e are very close. For $m_y(F_y)$, however, we find distinctly different d and e: Table 2.

From the 10 K neutron data we obtain $m_x(C_x) = 0.375\,\mu_B$, $m_y(F_y) = 0.895\,\mu_B$, $m_z(A_z) = 2.064\,\mu_B$, respectively. There seems to be a discrepancy between this value for $m_y(F_y)$ and the lower saturation value per Mn ion of only 0.17 μ_B derived from the magnetisation in a field of 100 Oe (Fig. 2). In the latter case, however, we measure a powder average in a field which is too small to flip all domain magnetisations so that they would have a nonzero component parallel to H. We have estimated the coercivity H_c from the ratio 0.17/0.895 and find $H_c \approx 60$ Oe, a value which compares well with direct measurements of the magnetisation cycle [29].

The magnetic moment at saturation $m_{total}(0\ K) = 2.27(0.02)\ \mu_B$ is well below the spin only estimation $\langle m_{total}\rangle = (1-x)m(t^3_{2g}e_g) + xm(t^3_{2g}) = 3.97\ \mu_B$ with $x = 0.9$. We will come back to this discrepancy in Section 4.

The m_x, m_y, m_z components depend differently on the temperature. Only m_z decreases monotonically between

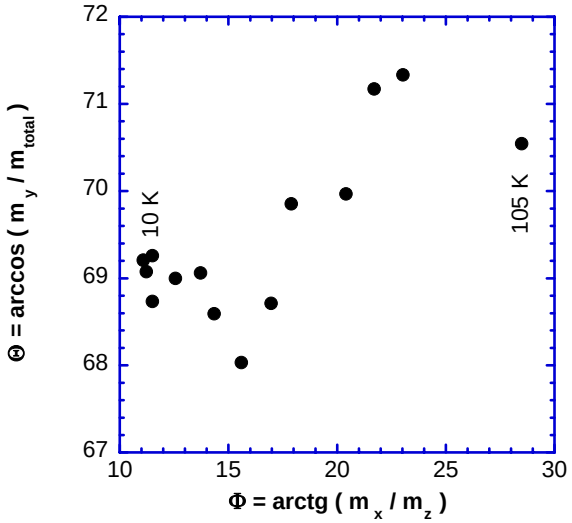

Fig. 6. The temperature dependence of the polar angles (Θ, Φ) of the local magnetisation. The polar coordinates (Θ, Φ) used refer to a coordinate system $(\xi, \eta, \zeta) = (z_{\rm cryst}, x_{\rm cryst}, y_{\rm cryst})$. The direction y of the ferromagnetic component is chosen as the polar axis.

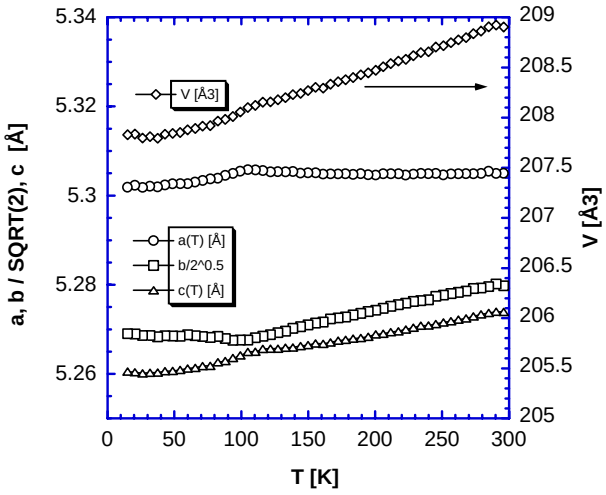

Fig. 7. The lattice constants $a(T)$, $b(T)$, $c(T)$ from X-ray data.

10 K and $T_{\rm N}$. The ferromagnetic component m_y stays effectively constant for 10 K $\leq T \leq$ 30 K, whereas m_x increases slightly from low temperatures up to 100 K and vanishes then within a narrow interval. This behaviour is a clear demonstration of spin rotation. In Figure 6 we describe the spin reorientation by the polar angles Θ, Φ defined by

$$\cos\Theta = m_x/m_{\rm total}$$
$$\tan\Phi = m_x/m_z,$$

i.e. with the ferromagnetic direction as the polar axis. We remark in passing that we do not find any hint for different critical temperatures for one or two of the three components of the Mn moments, as was found for one component in the canted antiferromagnetic insulator $La_{0.875}Sr_{0.125}MnO_3$ [32].

3.3 X-ray data: lattice constants and magnetoelastic effects

The data of the lattice constants a, b, c given in Figure 7 have been calculated by full profile refinement (SIMREF 2.4; [20]) X-ray diagrams comprising 100 reflections for each temperature. The onset of magnetoelastic distortions below 106 K is clearly visible. To separate thermal and magnetic effects we need an algorithm for the extrapolation of the $T > T_{\rm N}$ data into the magnetically ordered state. We have tried several methods. A polynomial extrapolation of the lattice constants b and c from the paramagnetic region gives reasonable results, it needs, however, additional and more or less arbitrary assumptions for the $a(T)$ constant as, for instance, a fixed value $a(0\ {\rm K})$ and/or a vanishing derivative at 300 K. A version of the Debye-Grüneisen theory of lattice expansion modified for orthorhombic symmetry along the lines suggested recently by Sayetat, Fertey and Kessler [33] did not produce stable results either, presumably due to the reduced temperature interval 110 K $\leq T \leq$ 300 K available for the extrapolation.

The analysis we present here is based on the observation, shown in Figure 8, that among the three areas $bc = A^2$, $ca = B^2$ and $ab = C^2$ two, namely A^2 and C^2, show only a minor magnetic influence at $T_{\rm N}$, or none at all. At lower temperatures the small deviations from the polynomial extrapolation are of the order of the error bars. The solid lines in Figure 8 have been determined from paramagnetic data using polynomials $P(T) = a_0 + a_2T^2 + a_3T^3 + a_4T^4$.

From A^2, B^2 and C^2 one obtains immediately $a = BC/A$, $b = CA/B$ and $c = AB/C$: Figure 9 demonstrates that these "model" lattice constants match the high temperature observations quite well. In Figure 10 we plot the magnetic excess lengths $-\Delta a$, Δb and $-\Delta c$. It is evident that the magnetic distortions $-\Delta a$ and Δb approach zero well below the Neel temperature whereas $-\Delta c$ vanishes at $T_{\rm N}$. This general behaviour is supported by all models of extrapolation, and also by fits of $-\Delta a$, Δb and $-\Delta c$ with equation (1).

Finally we present the thermal and magnetic strains defined here as $s_1 = (b/\sqrt{2} - c)/(b/\sqrt{2} + c)$, $s_2 = (c - a)/(c + a)$ and $s_3 = (a - b/\sqrt{2})/(a + b/\sqrt{2})$, again as a comparison between the calculated (from A, B, C) and the observed values (Fig. 11). s_2 is apparently not influenced by the magnetic order, whereas the magnetic contributions Δs_1 and Δs_3 have opposite signs, and at saturation $\Delta s_1(0\ {\rm K}) \approx -\Delta s_3(0\ {\rm K})$. We point out that the extrapolated component s_1 comes very close to zero at $T = 0$ K, and so, formally, the unit cell without magnetoelastic distortions would become metrically tetragonal.

We now look for correlations between the excess lengths and sublattice magnetisations. There is a clear correlation between the magnetic distortion $-\Delta c$ and the squared staggered magnetisation $m_z(A_z)$: Figure 12 shows the linear relation found. In complete analogy

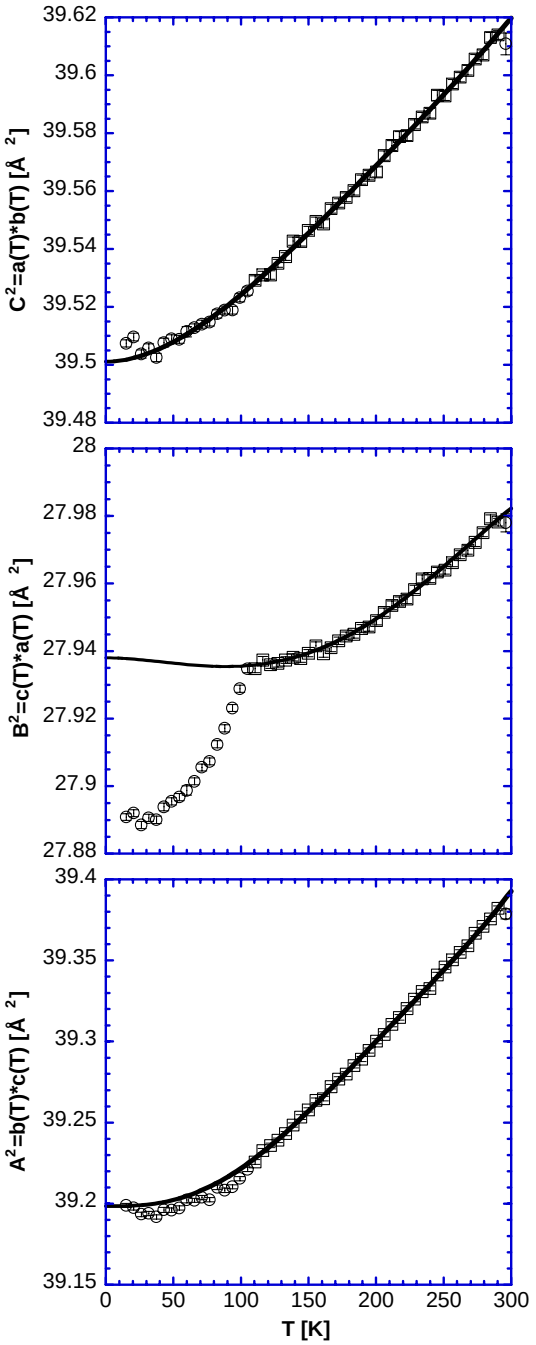

Fig. 8. The areas $A^2 = bc$, $B^2 = ca$, $C^2 = ab$. Only B^2 has a strong magnetoelastic contribution. Paramagnetic data (square symbols) have been used for the extrapolation to $T < T_N$ by polynomials $p(T) = a_0 + a_2T^2 + a_3T^3 + a_4T^4$.

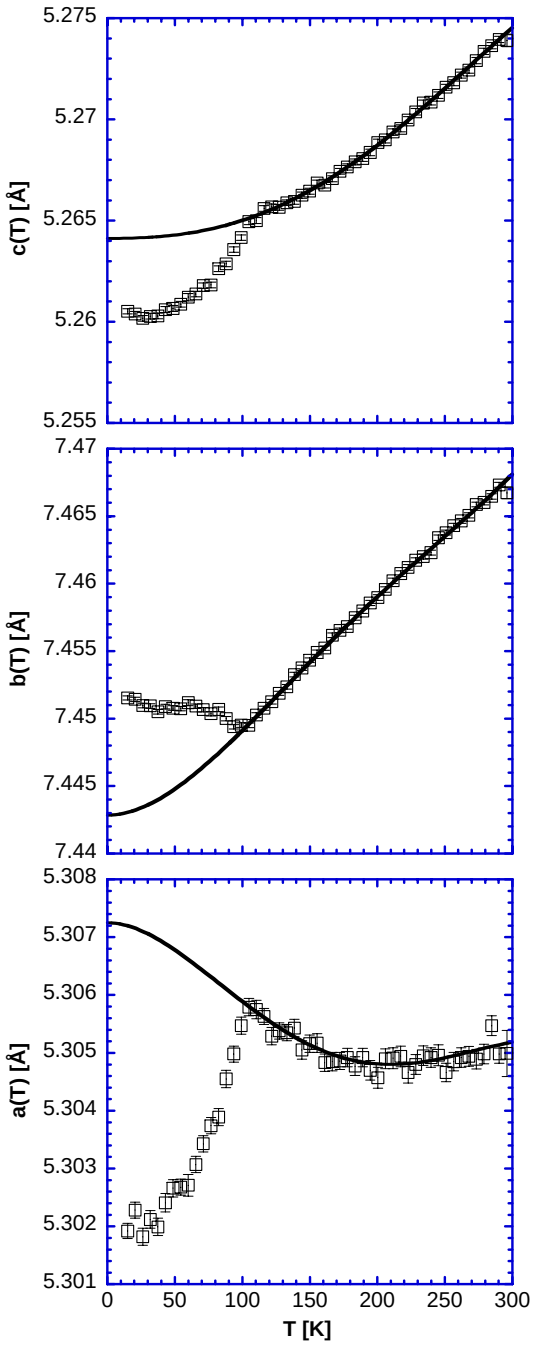

Fig. 9. The observed $a(T)$, $b(T)$, $c(T)$ compared with $a = BC/A$, $b = CA/B$, $c = AB/C$ calculated from the polynomial extrapolation in Figure 8.

with this the distortion $(-\Delta c)$ follows equation (1) with $d = 2.51(0.42)$ and $e = 0.87(0.10)$.

3.4 The microscopic distortions

We have analysed the real stoichiometry of our samples by diffraction. Four X-ray data sets collected with the Guinier diffractometer and one neutron diagram ($\lambda = 1.218$ Å), all measured at room temperature, were treated with SIMREF 2.4 [20]. The site occupation factors n for Ho/Ca, Mn and O found are: $n(\mathrm{Ho}) = 1 - n(\mathrm{Ca}) = 0.099(1)$, $n(\mathrm{Mn}) = 1.022(3)$, $n(\mathrm{O_1}) = n(\mathrm{O_2}) = 1.006(1)$.

We use a combination of the X-ray (lattice constants) and neutron data (oxygen coordinates) to follow the temperature dependence of the Mn-O distances and the Mn-O-Mn bond angles shown in Figures 13 and 14. In $Ho_{0.1}Ca_{0.9}MnO_3$ the *a priori* probability for Mn^{3+} and Mn^{4+} is 0.1 and 0.9, respectively,

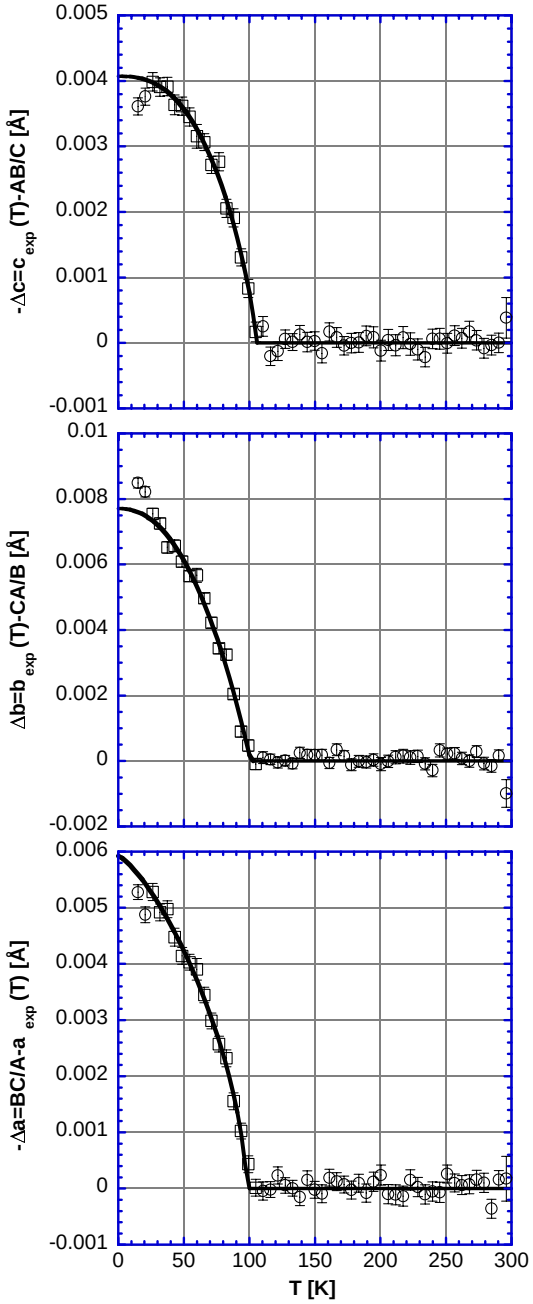

Fig. 10. The magnetic excess lengths $-\Delta a$, Δb, $-\Delta c$. Data (squares) in the magnetic temperature range are fitted by equation (1).

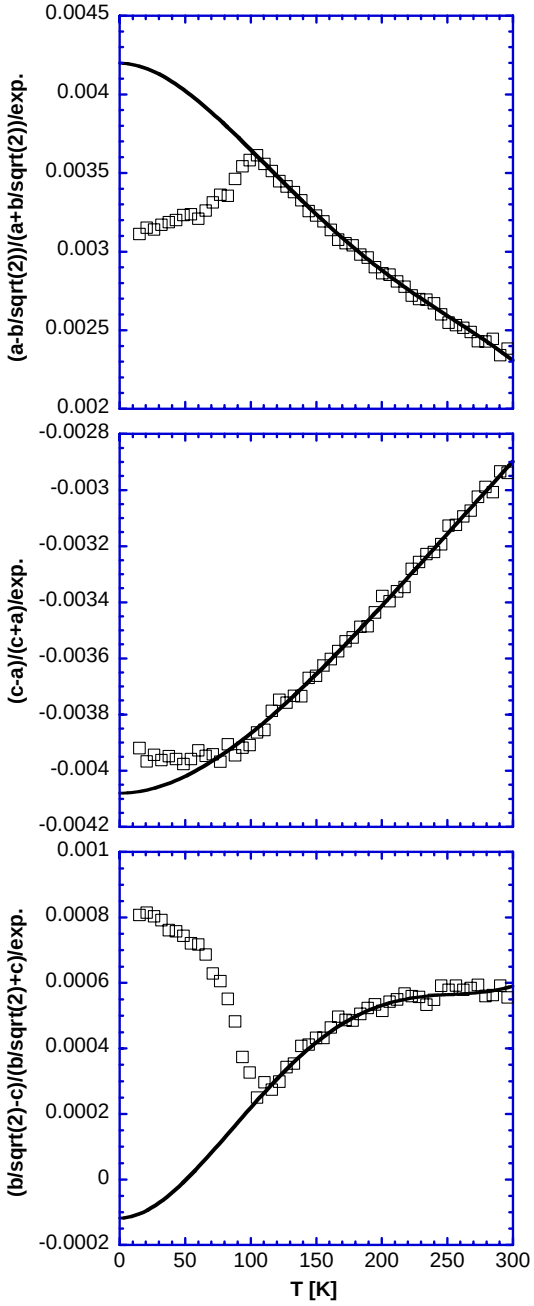

Fig. 11. The normalised thermal and magnetic strains $s_1 = (b/\sqrt{2}-c)/(b/\sqrt{2}+c)$, $s_2 = (c-a)/(c+a)$, $s_3 = (a-b/\sqrt{2})/(a+b/\sqrt{2})$.

and from the stoichiometric analysis just mentioned the actual Mn^{3+}/Mn^{4+}occupation factors are very close to 0.1/0.9. Since Bragg intensities always average over the whole lattice, all distances and bond angles given in Figures 13 and 14 are averages over the Mn^{3+}/Mn^{4+} disorder present. Nonetheless there is a clear evidence for the reduction of the (Mn-O)-(Mn-O) strain in the octahedra when the crystal enters into the magnetic state: Mn-O_{21} contracts by 1.25%, whereas Mn-O_{22} expands by 1.5%, and Mn-O_1 stays constant. Since the O_{21}-Mn-O_{22} plane coincides to within 10° with the *ac* plane (comp. Fig. 15), and Mn-O_1 deviates by nearly the same amount from the *b* direction, a homogeneous contraction of the octahedra would follow the behaviour of the lattice constants. This is, however, true only for Mn-O_1: as a consequence the angle Mn-O_1-Mn = Mn(0, 0, 0)-O_1-Mn(0, 1/2, 0) stays essentially constant between 10 K and 150 K: Figure 14. The second relevant bond angle Mn(0, 0, 0)-O_{21}-Mn(1/2, 0, −1/2) diminishes by roughly

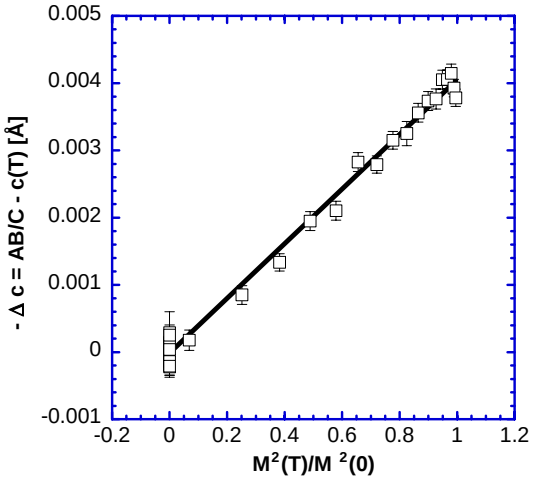

Fig. 12. The correlation between $-\Delta c$ and the normalised squared sublattice magnetisation of the $m_z(A_z)$ component.

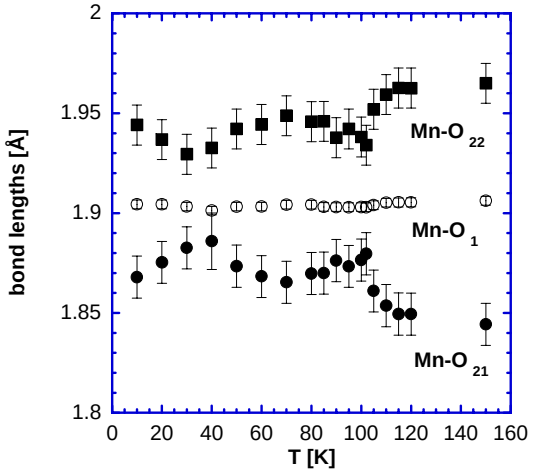

Fig. 13. Mn-O bond distances calculated from neutron and X-ray data. The difference in the distances $\Delta d = d_{\text{Mn-O}_{21}} - d_{\text{Mn-O}_{22}}$ is reduced by 50% during the transition from the paramagnetic into the ordered state. Here $O_1(x_1, y_1, z_1)$ and $O_{22} \equiv 2(x_2, y_2, z_2)$ are taken from Table 1, and O_{22} has the coordinates $(x_2 - 1/2, y_2, -z_2 - 1/2)$.

1° during the transition as a consequence of the magnetostrictive change of the area $B^2 = ca$ (Fig. 8).

4 Discussion

We discuss at first the orientation of the average magnetic moment with respect to the oxygen atoms surrounding manganese. At room temperature the MnO_6 octahedra are nearly regular with distances Mn-O_1, Mn-O_{21}, Mn-O_{22} found from a combination of one neutron ($\lambda = 1.218$ Å) and four X-ray data sets as 1.902 Å, 1.907 Å and 1.919 Å, respectively.

At 10 K the MnO_6 unit is essentially orthorhombic with distances 1.904 Å, 1.888 Å, 1.935 Å and angles (O_1-Mn-O_{21}), (O_{21}-Mn-O_{22}) and (O_{22}-Mn-O_1) of 89.7°, 89.7°

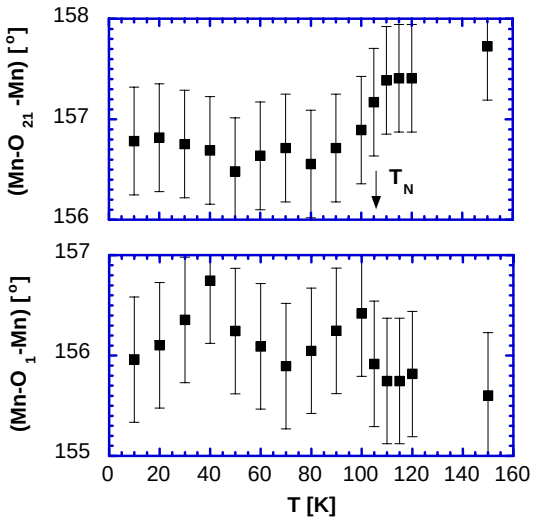

Fig. 14. The Mn-O_j-Mn bond angles Mn$(0,0,0)$-$O_1(x_1, y_1, z_1)$-Mn$(0, 1/2, 0)$, Mn$(0,0,0)$-$O_{21} \equiv O_2(x_2, y_2, z_2)$-Mn$(1/2, 0, -1/2)$. The angle Mn-$O_2$-Mn decreases by 1° between the paramagnetic and the magnetically ordered state.

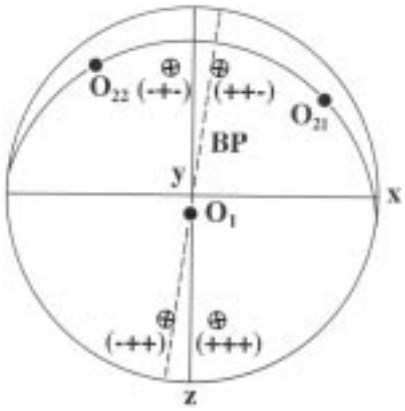

Fig. 15. A stereographic projection of the spin orientations $(+\,+\,+)$, $(-\,+\,-)$, $(+\,+\,-)$ and $(-\,+\,+)$ at the reference ion Mn in $(0,0,0)$ which are compatible with the neutron data. O_1, O_{21} and O_{22} belong to the oxygen octahedron surrounding Mn. BP is the plane which bisects the angle (Mn-O_{21}, Mn-O_{22}) and passes through Mn-O_1.

and 91.4°, respectively. The octahedra are, however tilted by $\approx 10°$ out of the ac plane, as shown in Figure 15. We may characterise these tilts more specifically by the angular deviations of Mn-O_1 from the direction b, and of Mn-O_{21} and Mn-O_{22} from the ac plane, for which we find, again at 10 K, 12.0°, 8.0° and 7.3°, respectively. In the ideal perovskite structure all these angles would be zero.

The magnetic components of the spin at Mn$(0,0,0)$ given in Table 1 are not unique, since any combination of signs in the local vector $(\pm|m_x|, \pm|m_y|, \pm|m_z|)$ produces the same magnetic intensities in experiments using unpolarized neutrons and zero external magnetic field: this is true for powder as well as single crystal specimens. The absolute values $|m_\alpha|$, $\alpha = x, y, z$, however, are unique.

Since a magnetic structure and its time reversed image are equivalent in $H = 0$, there remains a fourfold ambiguity of magnetic structures: $(\pm|m_x|, +|m_y|, \pm|m_z|)$ where the y-component has been fixed arbitrarily as positive. We refer these four models to the local orthogonal coordinate system of the reference Mn-O-octahedron. This is shown in Figure 15, where we use a shorthand notation, *e.g.* $(-+-)$ for $(-|m_x|, +|m_y|, -|m_z|)$. The deviations of the spin from the O_{21}-Mn-O_{22} plane are then $-32.0°$, $8.5°$, $11.0°$, $-31.5°$ for the $(+++)$, $(++-)$, $(-+-)$ and $(-++)$ configurations, respectively. The actual magnetic structure will be determined by the interplay of the exchange interactions and the local anisotropy tensors which both depend on the electronic configuration of the Mn ions contributing.

In the present series of neutron measurements we have reestablished also that undoped $CaMnO_3$ has a nearly pure collinear A_z structure. A very weak F_y component found from macroscopic magnetisation measurements [29] turned out to be below the detection limit of our neutron data. The origin of this small ferromagnetic component is likely to be due to oxygen defects [34]: an estimated deviation $\Delta c(O)/c(O) = 3 \times 10^{-3}$ in the oxygen stoichiometry is sufficient to explain this small contribution.

In $Ho_{0.1}Ca_{0.9}MnO_3$ the anisotropy responsible for the C_x and F_y components is due to the 10% admixture of $(t^3_{2g}e_g)/Mn^{3+}$. If we assume, tentatively, an appreciable anisotropy favoring O_{21}-Mn-O_{22} as the easy plane, then the configurations $(-+-)$ or $(++-)$ are expected to occur: the magnetic structure shown in Figure 3 with the local orientation $(++-)$ at $Mn(0,0,0)$ has been drawn under this assumption. At low temperatures the spin follows apparently the octahedral tilt: this is the influence of the electric multipolar fields dominated by nearest oxygen neighbours on the orbitals of the manganese ions.

Hopping e_g electrons are the origin of canted antiferromagnetism in mixed valent Mn^{3+}/Mn^{4+} compounds as well as for the metallic conductivity [3–5]. This concept has been extended recently [35] to include strong electron-phonon coupling contributions. We find indeed canted magnetic structures in $Ho_{1-x}Ca_xMnO_3$ for $0.825 \leq x \leq 1.0$ with a maximum of the ferromagnetic component close to $x = 0.9$ [29], and metallic conductivity for the same concentrations [30]. $Ho_{0.2}Ca_{0.8}MnO_3$ is already a pure collinear antiferromagnet [29].

There remains the question as to why Ho doping produces the strongest ferromagnetic composition with only 10% Ho, whereas for the prototype component $(La,Ca)MnO_3$ this optimum occurs at 60...75% La [1,2,36–39]. Further problems to be explained are the increase of the resistivity (Fig. 2) in $Ho_{0.1}Ca_{0.9}MnO_3$ at low temperatures as compared with the improving metallic behaviour in $La_{0.75}Ca_{0.25}MnO_3$ in the ferromagnetic state, and the small magnetic moment observed at the manganese ions in the ordered state.

(1) We first observe that the room temperature unit cell volume of $Ho_{0.1}Ca_{0.9}MnO_3$ is appreciably smaller than the volumes of the ferromagnetic isoelectronic series $(R_{0.7}B_{0.3})MnO_3$ with R = Y, La, Nd and B = Ca, Sr, Ba [41]: 208.98 Å^3 from the present data *vs.* 229.69 to 234.55 Å^3 [41].

(2) The Mn-O distances in $Ho_{0.1}Ca_{0.9}MnO_3$ in the magnetically ordered state for Mn-O_1, Mn-O_{21}, Mn-O_{22} are 1.905, 1.875, 1.940 Å (averaged over 10 K $< T <$ T_N in Fig. 13). In the paramagnetic state we find for the same distances 1.906, 1.843, 1.965 Å at 150 K, and 1.902, 1.907, 1.919 Å at 300 K: the time averaged orthorhombic distortions due to the Jahn-Teller effect increase between 300 K and 150 K, but decrease on entering the magnetically ordered state. The decrease of the strain component s_3 (Fig. 11) mirrors this effect. In $La_{0.75}Ca_{0.25}MnO_3$, however, Lanzara *et al.* [39] find 1.92, 1.92, 2.01 Å in the ferromagnetic metal against 1.92, 1.92, 2.01 Å and 1.91, 1.91, 2.13 Å for two different MnO_6 configurations in the colossal magnetic resistance state at $T > T^* \approx 220$ K. The reduced Mn-O bond lengths in the Ho compound quite evidently enhance the transfer integral [4,5] and improve electron hopping, *i.e.* delocalisation, and so a smaller abundance of $t^3_{2g}e_g$ configurations, again compared with $La_{0.75}Ca_{0.25}MnO_3$, gives rise to metallic behaviour and ferromagnetic canting. The lower population of $t^3_{2g}e_g$ results on the other hand in an only modest ferromagnetic component $m_y = 0.895\ \mu_B$. The reduction of the lattice averaged Jahn-Teller distortion in the magnetically ordered state (Fig. 13) is very likely due to a delocalisation of the e_g electrons in the form of magnetic polarons [40] with the concomitant increase of resistivity [41].

(3) The canting of the magnetic structure is reduced at Ho concentrations beyond 10% and vanishes at $\approx 17.5\%$ Ho. The reason is apparently an instability of the orthorhombic lattice against a monoclinic distortion (Pnma $\Longrightarrow P2_1/m$) which takes place for Ho concentrations beyond 13% [42], giving rise to partial charge order.

(4) We shall, at last, discuss the averaged magnetic moment of manganese. Basically the small space averaged magnetic moment observed in the magnetically ordered state might have two reasons: intraatomic effects or disorder.

On the atomic scale a low spin state of Mn^{3+} by strong crystalline fields, *i.e.* a transition from $t^3_{2g}e_g$ to t^4_{2g} can not be ruled out *a priori*. It would, however, be tied to a breakdown of Hund's rule for this configuration and the absence of Jahn Teller distortions, in contradiction with the observed orthorhombic distortion of the MnO_6 octahedra (Fig. 13). In addition even with all Mn^{3+} in the low spin state with $m_{Mn^{3+}\text{LOW SPIN}} = 3.18\ \mu_B$ the averaged magnetic moment would again be barely reduced to a mere $3.80\ \mu_B$, since the t^3_{2g} configuration of Mn^{4+} with a $^4A_{2g}$ ground state is not changed by strong crystal fields. So an intraatomic spin reduction can be safely excluded. An additional argument favoring normal magnetic behaviour on the atomic scale comes from the observed mean square averaged moment $\langle\mu^2_{Mn}\rangle^{1/2} = 3.3\ \mu_B$ as compared with the expected value $\langle\mu^2_{Mn\,theor}\rangle^{1/2} = 4.01\ \mu_B$. The difference

among these two values is very likely due to the approximation for the Ho contribution to $\chi(T)$ as explained in Section 3.2.

On the other hand there are two extreme cases for spin disorder. Firstly one may imagine the majority ions Mn^{4+} (90%) to be perfectly ordered in a planar antiferromagnetic $(C_x, 0, A_z)$ structure with the spin defects $(0, F_y, 0)$ at the random positions of the Mn^{3+} ions. Such a model is extremely unlikely because it does not provide any argument for a ferromagnetic order of the defect spins with a unique axis, since $(0, \pm F_y, 0)$ configurations are energetically equivalent in the $(C_x, 0, A_z)$ environment. Much more likely is a second model, a spin configuration in which the extra e_g electrons at Mn^{3+} provide for a directional polarisation of their Mn^{4+} neighbours in such a way that that the canted structure $(C_x(\mathbf{r}), F_y(\mathbf{r}), A_z(\mathbf{r}))$ changes smoothly close to a defect. The components C_x, F_y, A_z (Tab. 1, Fig. 4) observed from Bragg data are then the space averages $\langle C_x(\mathbf{r})\rangle$ etc., and the deviation from the spin only values will give rise to diffuse magnetic scattering which, in the presence of the paramagnetic scattering due to Ho^{3+}, would be hard to separate from powder data in the present case. This second model is the magnetic polaron picture introduced by Mott [40], and suggested for the manganites by Coey *et al.* [41]. Local charge neutrality demands that Mn^{3+} defects be close to the immobile Ho^{3+} ions, and this makes it likely that the polarons are localised but do overlap: a characteristic distance of 8 Å is estimated from the Ho^{3+} concentration. This has to be compared with the size of an MnO_6 octahedron of 3.9 Å (or 6.54 Å if one includes the oxygen electronic charge distribution). The overlap provides for a well defined direction of the ferromagnetic F_y component and for canting angles Θ_{ij} between neighbouring spins favoring electron hopping [5,41].

This extended defect picture is supported also by the observed Mn-O distances. In $Ho_{0.1}Ca_{0.9}MnO_3$ only 10% of the manganese ions are in the $t_{2g}^3 e_g$ configuration responsible for the Jahn-Teller distortion. The smooth transition from nearly undistorted octahedra at room temperature to the strong distortion at lower temperatures (Fig. 13) suggests a delocalisation of e_g electrons, since otherwise the majority (90%) of undistorted octahedra would dominate the scattering at low temperatures also, in contradiction with what we observe. A further hint towards this electronic effect comes from undoped $MnCaO_3$ with pure t_{2g}^3 configurations: we find at 10 K nearly undistorted octahedra with MnO-bond lengths of 1.882(0.003), 1.885(0.008) and 1.906(0.008) Å.

So, in summary, it is apparently the smaller ionic radius of Ho^{3+} as compared with La^{3+} which enhances electron hopping and the ferromagnetic coupling at low doping rates, but, destabilising the lattice at higher doping rates, gives rise to charge order in the monoclinic phase.

We acknowledge the support of this investigation by the BMBF and the DFG.

References

1. G.H. Jonker, J.H. van Santen, Physica **16**, 337 (1950).
2. J.H. van Santen, G.H. Jonker, Physica **16**, 599 (1950).
3. C. Zener, Phys. Rev. **82**, 403 (1951).
4. W. Anderson, H. Hasegawa, Phys. Rev. **100**, 675 (1955).
5. P.-G. de Gennes, Phys. Rev. **118**, 141 (1960).
6. E.O. Wollan, W.C. Koehler, Phys. Rev. **100**, 545 (1955).
7. R. von Helmholt, L. Haupt, K. Bärner, U. Sondermann, Solid St. Commun. **82**, 693 (1992).
8. R. von Helmholt, J. Wecker, K. Samwer, L. Haupt, K. Bärner, J. Appl. Phys. **76**, 6925 (1994).
9. S. Jin, T.H. Tiefel, M. McCormack, R.A. Fastnacht, R. Ramesh, L.H. Chen, Science **264**, 413 (1994); S. Jin, M. McCormack, T.H. Tiefel, R. Ramesh, J. Appl. Phys. **76**, 6929 (1994).
10. L.M. Rodriguez-Martinez, P. Attfield, Phys. Rev. B **54**, R15622 (1996).
11. J.M. De Teresa, M.R. Ibarra, J. García, J. Blasco, C. Ritter, P.A. Algarabel, C. Marquina, A. del Moral, Phys. Rev. Lett. **76**, 3392 (1996).
12. M. Kasai, H. Kuwahara, Y. Tomioka, Y. Tokura, J. Appl. Phys. **80**, 6894 (1996).
13. E.F. Bertaut, F. Forrat, J. Phys. Radium **17**, 129 (1956).
14. R.C. Vickery, A. Klann, J. Chem. Phys. **27**, 1161 (1957).
15. J.B. Goodenough, J.M. Longo, *Landolt-Börnstein*, edited by K.H. Hellwege, A.M. Hellwege (Springer Verlag; Berlin, Heidelberg, New York, 1970), Vol. III/4a, p. 126.
16. H.L. Yakel, W.C. Koehler, E.F. Bertaut, E.F. Forrat, Acta Cryst. **16**, 957 (1963).
17. A. Waintal, J. Chenavas, Mat. Res. Bull. **218**, 819 (1967).
18. J. Ihringer, W. Appel, Rev. Sci. Instrum. **55**, 1978 (1984); J. Ihringer, K. Röttger, J. Phys. D **26**, A32 (1993).
19. K.G. Lyon, G.L. Salinger, C.A. Swenson, J. Appl. Phys. **48**, 86 (1977).
20. J.K. Maichle, J. Ihringer, W. Prandl, J. Appl. Cryst. **21**, 22 (1988); H. Ritter, J. Ihringer, J. Maichle, SIMREF 2.4, Institut für Kristallographie, Universität Tübingen / available *via* internet: http://www.uni-tuebingen.de/uni/pki/simref/simref.html
21. D. Hohlwein, A. Hoser, W. Prandl, J. Appl. Cryst. **19**, 262 (1986).
22. A.M. Glazer, Acta Cryst. A **31**, 756 (1975).
23. *International Tables for Crystallography*, edited by T. Hahn, Vol. A (Reidel Publishing Company, Dordrecht, Holland 1983).
24. E.F. Bertaut in *Magnetism*, edited by G.T. Rado, H. Suhl, Vol. III, Chap. 4 (Academic Press, New York, 1963).
25. W. Opechowski, R. Guccione in *Magnetism*, edited by G.T. Rado, H. Suhl, Vol. IIa, Chap. 3 (Academic Press, New York, 1965).
26. J. Rodriguez-Carvajal, Physica B **192**, 55 (1993).
27. J.C. Le Guillou, J. Zinn-Justin, Phys. Rev. **39**, 95 (1977).
28. T. Oguchi, Phys. Rev. **117**, 117 (1960); F. Keffer, Handb. Phys. **XVIII/2**, 108 (1966).
29. H. Schmid, J. Ihringer, K. Knorr, W Prandl, H. Ritter, T. Zeiske, J. Magn. Soc. Jap. **23**, 525 (1999).
30. K. Knorr, W. Prandl (to be published).
31. J. Adler, Solid State Phys. **21**, 193 (1968).
32. D.N. Argyriou, J.F. Mitchell, C.D. Potter, D.H. Hinks, J.D. Jorgensen, S.D. Bader, Phys. Rev. Lett. **76**, 3826 (1996).

33. F. Sayetat, P. Fertey, M. Kessler, J. Appl. Cryst. **31**, 121 (1998).
34. A. Reller, J.M. Thomas, D.A. Jefferson, M.K. Uppal, Proc. Roy. Soc. London A **394**, 223 (1984).
35. A.J. Millis, P.B. Littlewood, B.I. Shraiman, Phys. Rev. Lett. **74**, 5144 (1995).
36. P.G. Radaelli, D.E. Cox, M. Marezio, S.-W. Cheong, P.E. Schiffer, A.P. Ramirez, Phys. Rev. Lett. **75**, 4488 (1995).
37. P. Schiffer, A.P. Ramirez, W. Bao, S.-W. Cheong, Phys. Rev. Lett. **75**, 3336 (1995).
38. P.G. Radaelli, M. Marezio, H.Y. Hwang, S.-W. Cheong, B. Batlogg, Phys. Rev. B **54**, 8992 (1996).
39. A. Lanzara, N.L. Saini, M. Brunelli, F. Natali, A. Bianconi, P.G. Radaelli, S.-W. Cheong, Phys. Rev. Lett. **81**, 878 (1998).
40. N.F. Mott, *Metal-Insulator Transitions* (Taylor & Francis, London, 1974).
41. J.M.D. Coey, M. Viret, L. Ranno, K. Ounadjela, Phys. Rev. Lett. **75**, 3910 (1996).
42. H. Ritter, K. Burger, D. Hohlwein, J. Ihringer, K. Knorr, W. Prandl, Th. Zeiske, Z. Krist. Suppl. **15**, 112 (1998).